19th AIAA Computational Fluid Dynamics
22 - 25 June 2009, San Antonio, Texas

AIAA 2009-4146

Shock/Boundary Layer Interaction Effects of Transverse Jets in Crossflow over a Body of Revolution

Dean A. Dickmann*
Lockheed Martin Missiles and Fire Control, Grand Prairie, Texas, 75265

and

Frank K. Lu†
University of Texas at Arlington, Arlington, Texas 76019

Shock/boundary layer interaction present in transverse jets in supersonic crossflow alteres the mean flow in the near field by bifurcating the phase portrait of the separation topology. This study discusses the results of numerical simulations investigating the mean flow field in the near field of a jet issuing perpendicular to a flat plate and a body of revolution. The results show the interaction between the jet and the supersonic freestream is affected by the shape of the body. The addition of an attachment node at the tip of the nose of a body of revolution altered the flow structure by eliminating the second pair of horseshoe vortices leaving only one pair of horseshoe vortices. The presence of the additional attachment node, not only affected the mean flow structure, but also modified the surface pressure distribution and, ultimately, the performance coefficients.

Nomenclature

$\overline{C}_f$	= transformed skin friction coefficient (ref. 19)	$\overline{Re}_\theta$	= transformed Reynolds number (ref. 19)
C_m	= pitching moment coefficient	T	= temperature
C_N	= normal force coefficient	u^+	$= \sqrt{\frac{2}{C_{fw}}\frac{T_\delta}{(T_w - T_\delta)}}\sin^{-1}\left(\frac{u}{u_\delta}\sqrt{1-\frac{T_\delta}{T_w}}\right)$ (Ref. 18)
C_T	= thrust coefficient, $= F/(q_\infty S_{ref})$	x	= streamwise Cartesian coordinate
d	= diameter	y	= normal direction
l, L	= length	y^+	$= \frac{p_w y u_\delta}{R_g T_w}\frac{(T_w + C_2)}{C_1 T_w^{1.5}}\sqrt{\frac{T_w}{T_\delta}\frac{C_{fw}}{2}}$ (Ref. 18)
M	= freestream Mach number	z	= spanwise direction
p	= pressure	ε	= amplification coefficient
PR	= pressure ratio	η	$= \frac{y}{x}\sqrt{\frac{\rho_\infty u_\infty x}{\mu_\infty}}$ (Ref. 18)

Subscripts			
jet	= jet exit	x	= x-direction
ji	= jet interaction	ref	= reference
		t	= total

* Senior Staff Engineer, Systems Engineering Department, Member AIAA.
† Professor and Director, Aerodynamics Research Center, Mechanical and Aerospace Engineering Department, Box 19018. Associate Fellow AIAA.

Copyright © 2009 by Dr. Dean A. Dickmann. Published by the American Institute of Aeronautics and Astronautics, Inc., with permission.

I. Introduction

JETS issuing perpendicularly to a freestream have been the subject of research for more than sixty years.[1] Much of the research has been focused on vertical/short take-off and landing applications, where the freestream is either quiescent or regarded as incompressible, or scramjet engine applications where mixing is the primary concern. Reaction jet control systems (RJCS) have received less attention, but have gained focus recently as vehicle maneuverability requirements have increased. The interest in RJCS applications is directed at the surface pressure perturbations caused by the interaction between the jet and freestream, generally referred to as jet interaction (JI), which can alter the effectiveness of the RJCS. Ferrari[2], Spaid[3] and Spaid and Cassel[4] have suggested a transverse jet in crossflow can be represented by a solid body of given length and shape in inviscid flow. Observations have revealed this simplistic model is not realistic because it does not include plume overexpansion, proper vortex generation or the proper separation topology. Current understanding of the near field mean flow structure in a supersonic freestream due to Morkovin, et al.,[5] Cubbison,[6] Fric and Roshko[7] and Roger and Chan[8] has been described and illustrated by Champigny and Lacau.[9] This mean flow structure has been confirmed by Gruber, et al.[10] and is widely accepted by most researchers.

The mean flow structure depicted by Champigny and Lacau is shown in Figure 1. Among the features of this model are the λ-shock structure upstream of the jet created by the interaction between the bow shock and approaching boundary layer, the subsequent three-dimensional separation zone wrapping around the jet and the counter-rotating jet vortices. In addition to these features, the following features are also present: a barrel shock around the plume terminating in a Mach disk, horseshoe vortices convecting around the jet and a downstream secondary shock. The current study seeks to verify these flow structures for a flat plate via numerical simulations, examine changes in these flow structures for a body of revolution and identify amplification effects on the jet thrust for both geometries.

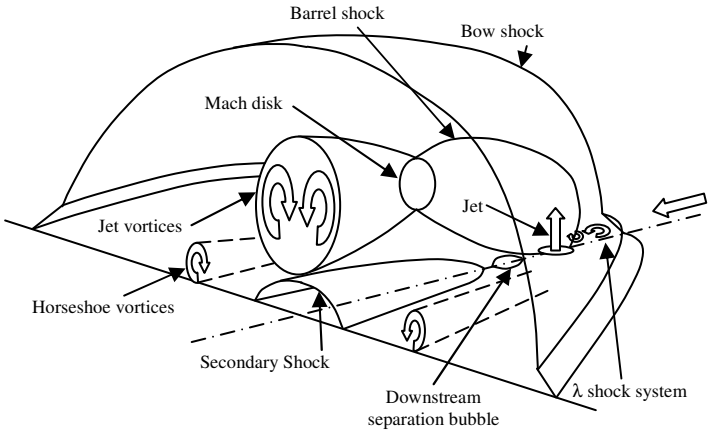

Figure 1. Currently accepted near field mean flow structure.

The three-dimensional viscous-inviscid interaction present in supersonic JI precludes the use of many simplifying assumptions. Without these simplifying assumptions, a three-dimensional Reynolds-averaged Navier-Stokes (N-S) solver was required to simulate the interaction. Two solvers were evaluated for this application, namely, Falcon, a Lockheed Martin code, and GASP, a commercial code[11]. These codes were exercised to determine the ability of each to properly simulate the near field mean flow structure. The evaluation concluded Falcon with a *k-kl* turbulence model[12] was the more appropriate numerical model.

II. Preliminary Flow Simulations

Falcon solves the full set of unsteady three-dimensional conservation equations[13] with Reynolds and Favre averaged quantities by marching the equations through time (or pseudo-time) to a steady-state solution. Details of the code can be found in Ref. 11. In this section, a limited validation of the code pertinent to the present study is provided. This validation was performed against data for undisturbed supersonic turbulent flow over a flat plate and supersonic turbulent flow over a flat plate with a transverse jet of pressure ratio 308. Further validation for a wide variety of flows can be found in Ref. 12.

II.1 Undisturbed Turbulent Boundary Layer

Falcon was applied to undisturbed turbulent flow over a flat plate at Mach 2.23 and 4.5. The results are compared against the data of Shutts, et al.[14] and Mabey, et al.[15] as compiled by Fernholz and Finley[16] in Figs. 2 and 3. Figures 2 and 3 show the boundary layer velocity profiles in wall coordinates[17] at two locations along the plate for the numerical calculations, the experimental data and the law-of-the-wall profiles.[18]

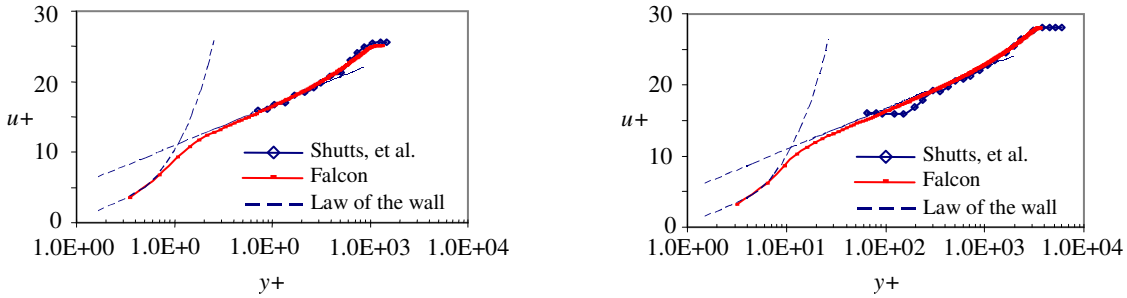

a. $x = 0.193$ m. b. $x = 0.802$ m.

Figure 2. Comparison with Shutts et al.'s data at $M = 2.23$, $Re_x = 25 \times 10^6$/m.

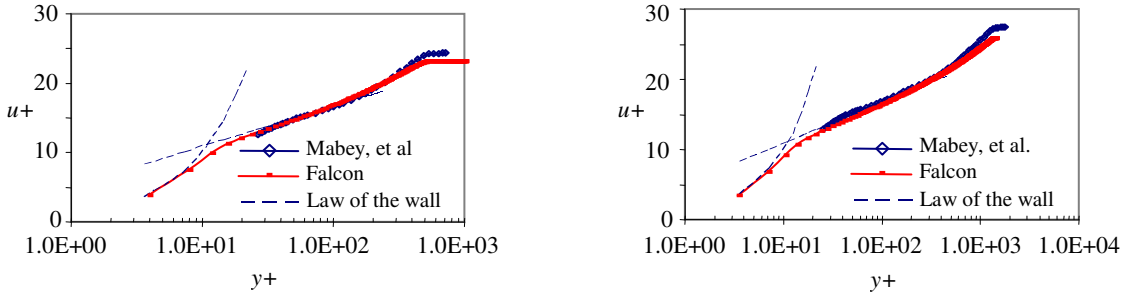

a. $x = 0.368$ m. b. $x = 1.384$ m.

Figure 3. Comparison with Mabey et al.'s data at $M = 4.5$, $Re_x = 28.1 \times 10^6$/m.

The numerically computed results matched the experimental and law-of-the-wall data well at both Mach 2.23 and 4.5 in the logarithmic and wake regions at both axial locations. Further evaluation of the solvers was done by examining the local skin friction coefficients. These coefficients are compared in Fig. 4. Hopkins and Inouye[19] recommended the Van Driest II (VDII) transformation of the skin friction coefficient as the best possible method for transforming turbulent compressible flow to the incompressible plane for comparison with the Karman-Schoenherr (K-S) equation (Eq. 3 in Ref. 19). Figure 4 plots the transformed test data, the transformed computational results and the K-S equation. The computational results compared well with test data and the K-S equation at Mach 2.23 but showed some discrepancy from both at Mach 4.5.

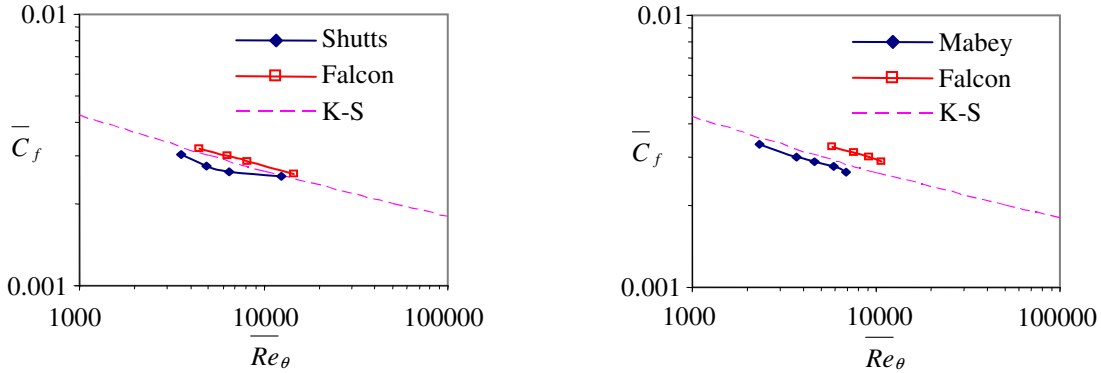

a. Mach 2.23. b. Mach 4.5.

Figure 4. Local skin friction coefficient.

II.2 Transverse Jet in Supersonic Crossflow with a Turbulent Boundary Layer

This section presents computational results compared to experimental data from Dowdy and Newton.[20] Dowdy and Newton collected a significant amount of surface pressure data on flat plates in supersonic crossflow that have a jet issuing into the stream perpendicularly. Falcon was applied to the test conditions listed in Table I. The results of the numerical simulation are plotted in Figure 5.

Table I Dowdy and Newton test conditions.

M	2.61	$T_{t\infty}$ (R)	564.67
p_{tjet} (psf)	43214.4	d_{jet} (in.)	0.1
T_{tjet} (R)	533.67	L_{plate} (in.)	18
p_∞ (psf)	140.54	W_{plate} (in.)	7.5

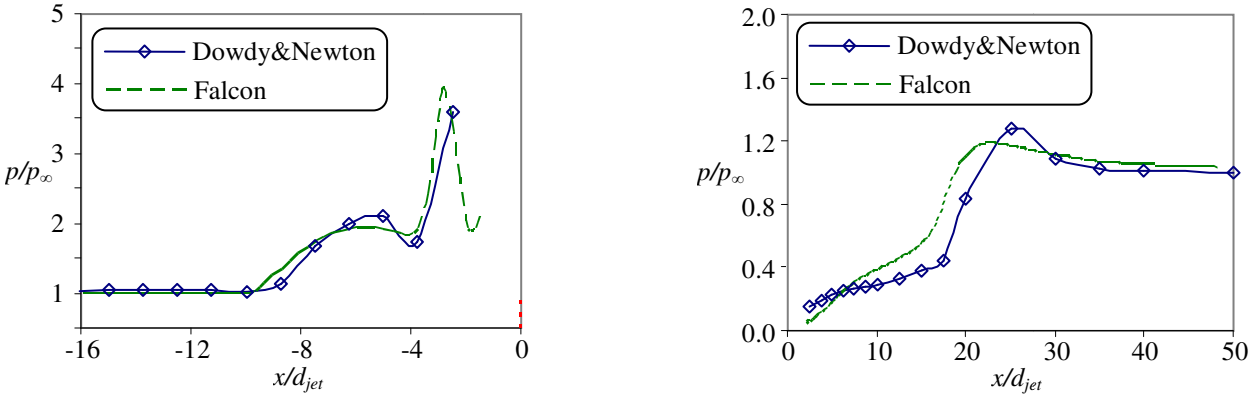

a. Upstream pressure distribution. b. Downstream pressure distribution.

Figure 5. Upstream pressure distribution comparison.

The resulting pressure distributions upstream and downstream of the jet along the centerline of the plate are compared with data from Dowdy and Newton in Fig 5. In Figure 5, the pressure is normalized by the ambient pressure while the distance along the plate is normalized by the diameter of the jet, d_{jet}, with the upstream distribution shown in Fig. 5a and the downstream shown in Fig. 5b. The diamond symbols represent the experimental data[20] and show the upstream pressure calculations from Falcon shown by the dashed line agreed well with experimental data.

The experimental data in Figure 5b show a massive overexpansion of the highly underexpanded jet (*PR*=308) to below 10% of ambient. The overexpansion is followed by a gradual recompression until the pressure overshoots ambient before expanding back to ambient. The computations captured the overexpansion, but overpredicted the slope of the recompression and underpredicted the overshoot. Nonetheless, Fig. 5 shows the computations can provide reasonable results for transverse jets in a supersonic freestream.

III. Results and Discussion

In this section, results of a numerical simulation of a transverse jet with pressure ratio 2000 issuing into a Mach 2 freestream over a flat plate are compared with results of a jet with the same properties issuing into a Mach 2 freestream over a body of revolution. The flat plate is 457.2 mm square with a jet orifice located on the centerline, 177.8 mm from the leading edge and was analyzed with the coordinate system shown in Fig. 6. The jet issued from the convergent nozzle shown in Fig. 7, dimensions are in millimeters.

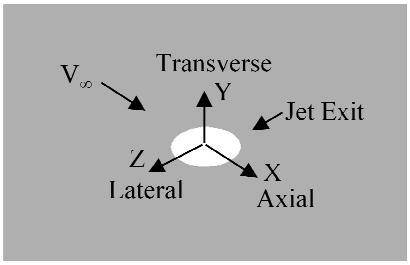

Figure 6. Flat plate coordinate system.

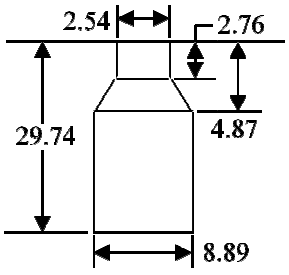

Figure 7. Convergent nozzle configuration (dimensions in mm).

The body of revolution is a cylindrical body preceded by a 3:1 Von Karman nose with a spherical tip as shown in Figure 8. The jet issued from the same convergent nozzle shown in Figure 7 at 150.4 mm from the tip of the nose. The total pressure at the inlet of the nozzle for both geometries was 19665.2 kPa (410717.6 psf). The jet issued into a freestream with an ambient pressure of 9.83 Pa (205.4 psf) yielding a *PR* = 2000.

Comparison of the FP and BOR results highlights the effect of body geometry on the near field mean flow structure of transverse jets in supersonic freestreams. Figure 9 shows streamlines exiting the nozzle of the BOR and streamlines exiting the nozzle of the FP.

The BOR streamlines spread in a similar manner to the FP streamlines, but with slightly more downstream inclination. This similarity implies similar wave formations upstream of the jet as shown in Figure 10. Figure 10a shows velocity vectors and pressure contours on the centerplane of the FP domain while Figure 10b shows velocity vectors and pressure contours on the centerplane of the BOR.

Figure 8. Body of Revolution (BOR) (in mm).

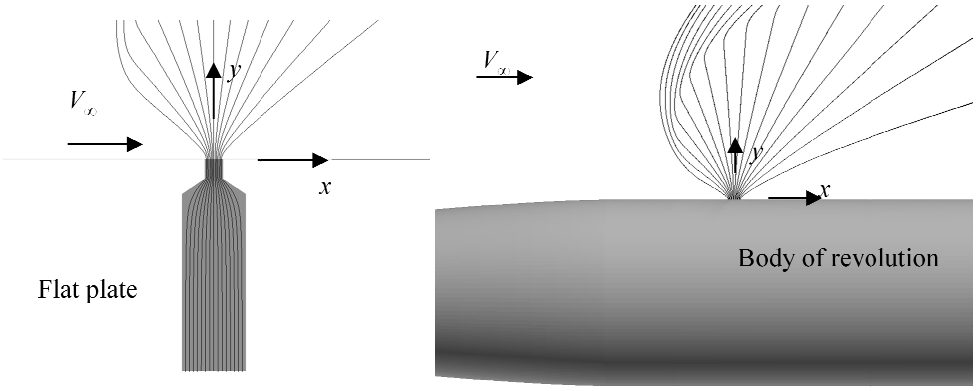

Figure 9. Streamline comparison, FP and BOR.

The basic flow structures for both the FP and BOR are similar and Figure 11 shows a sketch of the wave formations present in the interaction upstream of the jet for the both geometries.

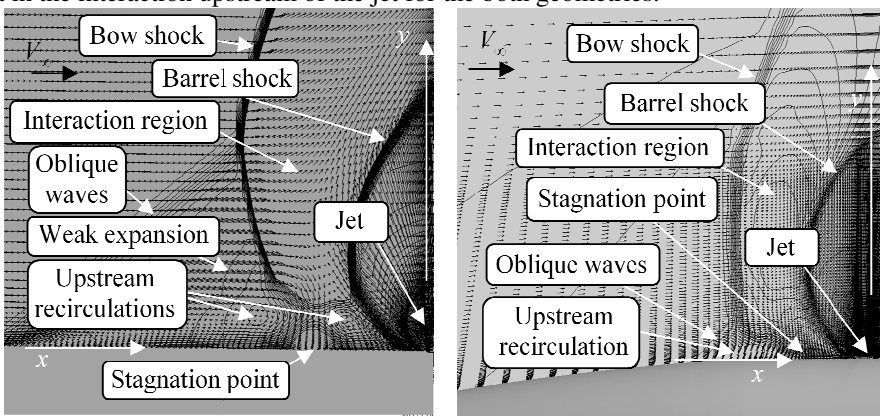

a. Flat Plate (FP). b. Body of Revolution (BOR).

Figure 10. Upstream pressure contours and velocity vectors.

The highly underexpanded jet emerged from the nozzle, in the bottom right corner of Fig. 10a and b, obstructing the freestream approaching from the left. The obstruction deflected the supersonic freestream in the transverse and lateral directions generating a three-dimensional shock wave, typically referred to as the bow shock. The bow shock interacted with the approaching boundary layer to create a complex inviscid/viscous interaction known as a shock/boundary layer interaction with a λ-shock structure.[21] As the bow shock intersected the boundary layer, the boundary layer sensed the pressure rise across the shock altering the viscous velocity profile and thickening the boundary layer as shown in Fig. 11a and b. As the shock penetrated the boundary layer, it refracted downstream due to the change in the Mach number through the boundary layer. For the flat plate, shown in Fig. 11a, the refracted shock turned a portion of the boundary layer flow toward the surface creating a node of attachment (or stagnation point) and an adverse pressure gradient that separated the boundary layer from the surface upstream of the node and created the upstream saddle point. As will be shown later, this saddle point originated a pair of separation lines and a separation zone between the freestream and the jet.

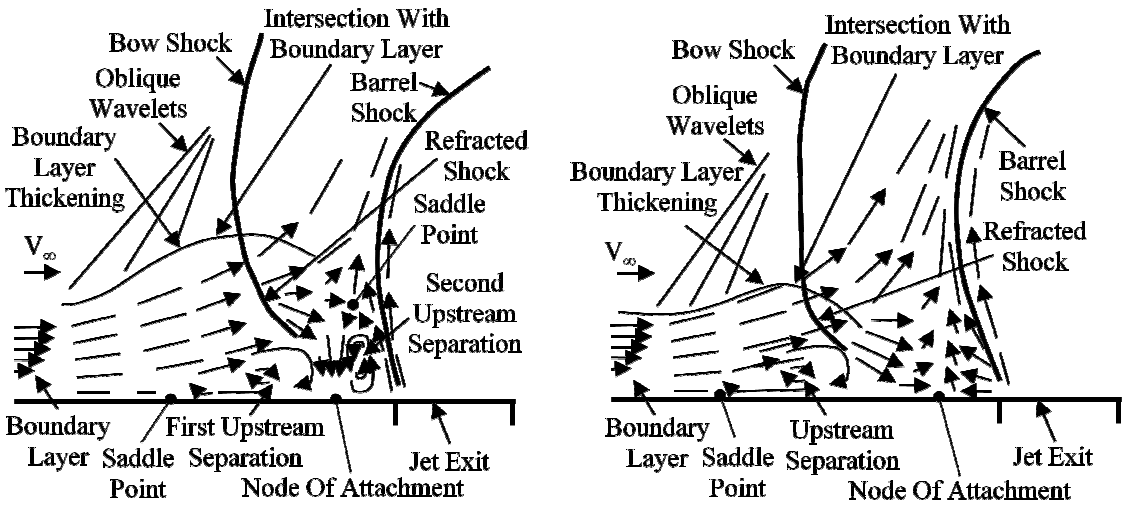

a. Flat Plate b. Body of Revolution

Figure 11. Sketch of interactions.

Within the separation zone, the node of attachment on the flat plate divided two recirculation regions as shown in Fig. 11a. The flow to the left of the node turned into an upstream recirculation between the upstream saddle point and node. The flow to the right turned toward the jet, deflected immediately upward into a saddle point within the interior of the flow then turned back toward the attachment node.

For the BOR, the bow shock was refracted less through the boundary layer than the FP geometry. The refraction is less because the Mach number in the flow field downstream of the nose shock was reduced. The portion of the boundary layer that was turned by the less refractive shock realigned with the wall before interacting with the jet flow. The interaction between the jet flow and the realigned boundary layer created a node of attachment, but not a second recirculation as shown in Fig. 11b.

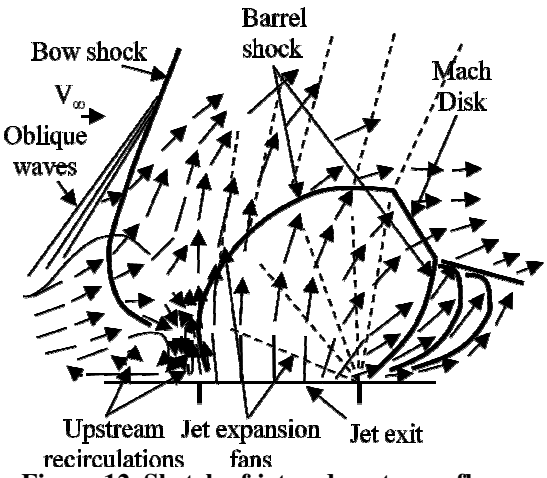

Figure 12. Sketch of jet and upstream flow structure, $M = 2.0$.

For both the FP and BOR geometries, Fig 11a and b show that outside the recirculation regions, upstream of the saddle point, the thickened boundary layer produced oblique compression waves which coalesced into the bow shock, creating the upstream leg of the λ. The refracted bow shock completed the λ-shock structure which dominated the near field flow structure upstream of the jet and dramatically impacted the jet trajectory. The strength of the λ-shock bent the jet approximately 30° downstream. As the jet was turned, an oblique shock wave formed within the jet, typically referred to as the barrel shock, which propagated across the jet as illustrated in Fig. 12.

As the barrel shock traveled across the jet, expansion waves emanating from the leeward edge of the jet exit intersected the barrel shock bending it downstream. These expansion waves deflected as they passed through the barrel shock generating an expansion fan in the interaction region which turned the freestream around the jet. As the jet turned downstream, separation foci (discussed later) turned the leeward side of the barrel shock away from the surface toward the windward side of the barrel shock. The deflection of the leeward side of the barrel shock exceeded the maximum allowable deflection for an attached shock resulting in the formation of a normal shock between the windward and leeward sides of the barrel shock, the so-called Mach disk. The reflected shock emanating from the Mach disk on the leeward side coalesced with compression waves generated by the downstream separation zone (discussed later) as it moved downstream to intersect the FP surface. No reflected shock emanated from the windward side of the Mach disk because the intersection of the expansion waves with the windward side of the barrel shock aligned the streamlines to the wall.

These flow characteristics produced by the presence of these waves are a result of the fundamental inability of pressure disturbances to propagate upstream in supersonic flow (except through the thin subsonic region near the surface). In no better way can these complex characteristics be illustrated than in Fig. 13 and 14 where skin friction lines are plotted with surface pressure contours for both FP and BOR geometries.

Figure 13 show skin friction lines in black and surface pressure contours in white with the salient features of the separation topology[22] highlighted for the FP. Figure 13 shows four saddle points, two attachment nodes and one node of separation with four pairs of global separation lines. This arrangement of features is typically referred to as the phase portrait[22]. The pair of global separation lines emanating from the saddle point furthest upstream of the jet moved downstream, separated by nearly 7 jet diameters. These separation lines proceeded downstream without ever converging to a node or focus. Without this convergence, a large portion of the plate was covered by the separation zone.

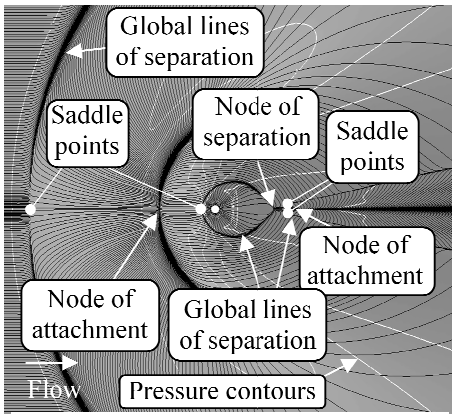

Figure 13. Skin friction lines around jet, FP

The phase portrait for the BOR is shown in Fig. 14. This figure shows the FP and BOR had similar phase portraits, but the BOR has an additional attachment node at the nose tip not shown in Fig. 14. In this case, the pair of global separation lines emanating from the saddle point furthest upstream of the jet wrapped around the body without converging. Without this convergence, a large portion of the body was covered by the separation zone. As will be shown later, this affected performance compared to the flat plate because a component of the force produced by the pressure perturbations on left and right sides of the body canceled.

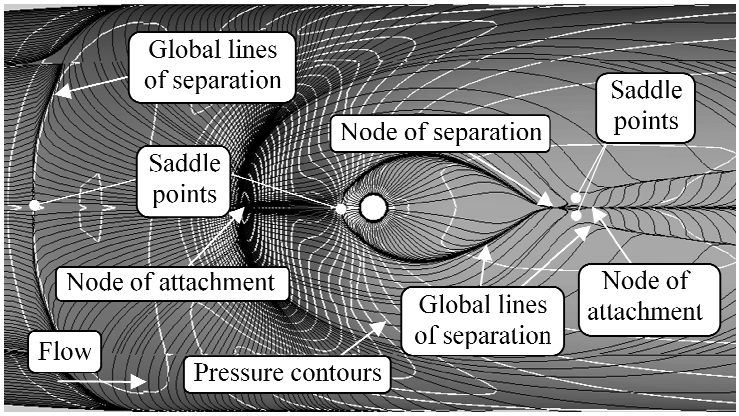

Figure 14. Skin friction lines around jet, BOR

For both geometries, a second global line of separation emanated from the second upstream saddle point, wrapped around the jet and converged on the node of separation downstream of the jet. A third and fourth pair of global separation lines emanated from each of the downstream saddle points as mirror images. In each pair, one separation line intersected the node of separation and the other propagated downstream.

In both cases, the combination of the upstream saddle points and the node of attachment provided the necessary topology to generate horseshoe vortices. Figure 15 shows the saddle points and attachment node spawned two sets of horseshoe vortices.

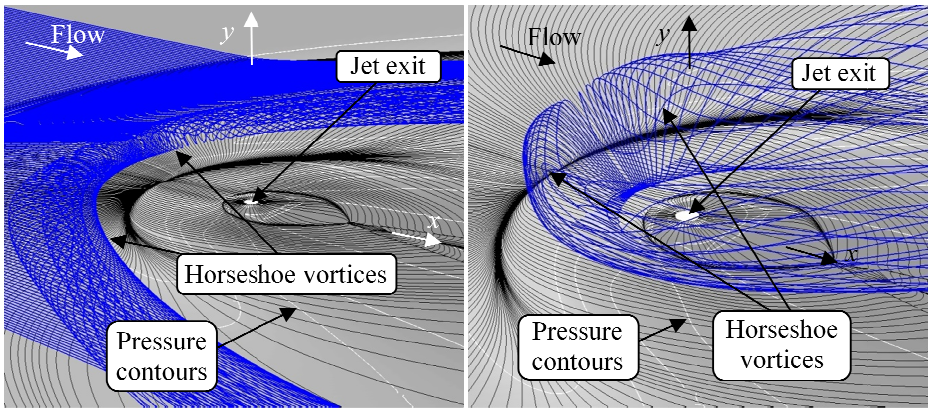

a. First horseshoe vortices b. Second horseshoe vortices

Figure 15. Horseshoe vortices, FP.

Figure 15a shows streamlines coiling up into the first set of horseshoe vortices as they follow the dividing surfaces of the first set of global separation lines around the jet into the separation zone with skin friction lines in black and surface pressure contours in white. The streamlines wrapped under each other producing a *clockwise* left running vortex and the *counterclockwise* right running vortex. These vortices convected around the jet, bent downstream and remain a flow structure to the end of the plate.

Figure 15b shows streamlines coiling up into the second set of horseshoe vortices following the dividing surfaces emanating from the second set of global separation lines. These streamlines rotate opposite to the first set of horseshoe vortices producing a *counterclockwise* left running vortex and a *clockwise* right running vortex. Unlike the first set of vortices, this set of vortices convected into the flow of the jet. Since these vortices convect into the jet, they only effected the upstream surface pressure distribution.

As previously mentioned, only one set of horseshoe vortices were present on the BOR. The upstream recirculation resulted from the combination of the attachment node and the first saddle point in the near field. The saddle point closer to the jet acted in combination with the attachment node at the nose tip. With this saddle point downstream of its attachment node, the pressure gradient was favorable so no recirculation or horseshoe vortices were generated. The result was a single set of horseshoe vortices in the massive separation around the jet as shown in Figure 16.

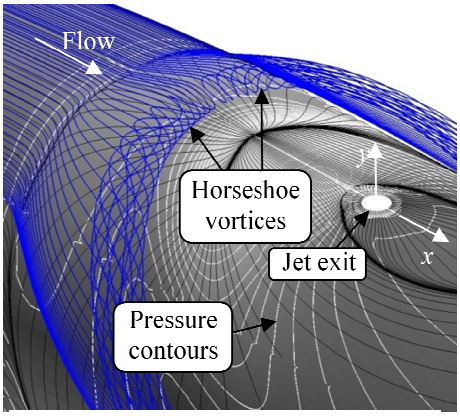

Figure 16. Horseshoe vortices, BOR

Figure 16 shows streamlines coiling up into horseshoe vortices similar to those on the FP. These vortices convected around the jet, bent downstream and around the body and remained a flow structure to the end of the body.

Downstream of the jet, the combination of the saddle points, node of attachment and node of separation generated two sets of vortices as shown in Figure 17 for the FP.

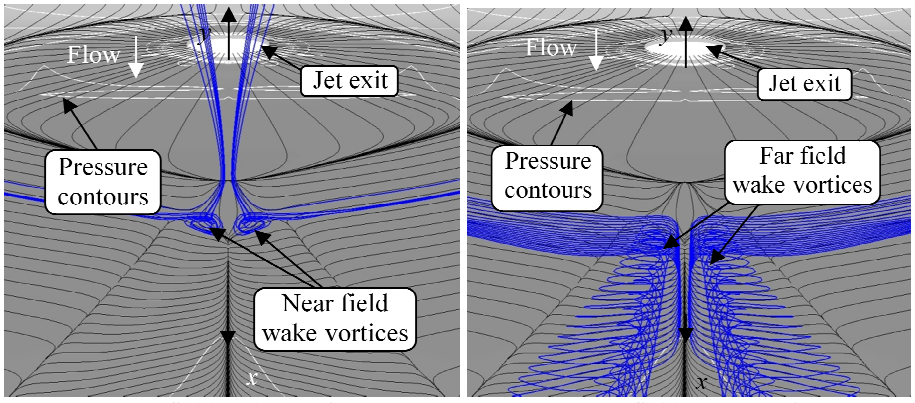

a. Near field wake vortices b. Far field wake vortices

Figure 17. Wake Vortices, FP.

Streamlines following the dividing surface emanating from the global separation lines between the saddle points and the node of separation (shown in Fig. 13) wrapped into a set of near field wake vortices as shown in Figure 17a for the FP. The left running vortex rotating *clockwise* and the right running vortex rotating *counterclockwise* of the near field wake vortices were carried by the dividing surfaces *upstream* toward the jet until they were turned vertically by the separation node and became entrained in the jet. The streamlines following the dividing surface emanating from the global separation lines propagating downstream from the saddle points wrapped into a set of far field wake vortices as shown in Figure 17b. The left running vortex rotated *clockwise* and the right running vortex rotated *counterclockwise* convecting *downstream* away from the jet persisting to the end of the plate.

For the BOR only far field wake vortices were detectable even though the topology was the same for both the FP and the BOR. It was reasoned the near field wake vortices were present, but were so small they could not be resolved by the grid and thus considered negligible. In the same fashion as the FP, far field wake vortices followed the dividing surface downstream with the left running rotating *clockwise* and the right running rotating *counterclockwise*.

These flow structure and separation topologies are manifested in perturbations to the surface pressures near the jet. Examination of the surface pressure distributions are shown in Figs. 18a and b.

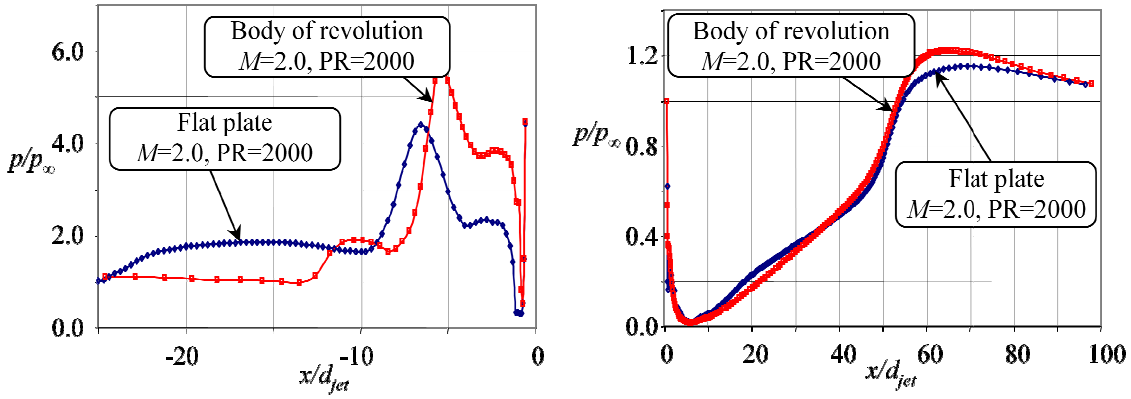

a. Upstream of jet. b. Downstream of jet.

Figure 18. Streamwise surface pressure distribution along centerline axis, *PR* = 2000.

Figure 18 shows normalized surface pressures plotted against the normalized axial distance upstream and downstream of the jet for both the BOR and FP. Figure 18a shows the characteristics of the pressure distributions are similar. By comparing the distributions at equivalent upstream locations, it is seen the initial pressure rise occurred further downstream on the body than the flat plate. The positive pressure gradient on the nose of the body allowed the boundary layer to penetrate further into the adverse pressure gradient created by the jet than the flat plate boundary layer. After the initial pressure rise, caused by the oblique wavelets of the λ shock, there was a slight depression caused by the recirculation followed by a peak at the attachment node and an expansion thereafter into the barrel shock. It can be seen in Figure 18a that the stagnation pressure and the surface pressures downstream of the attachment node for the BOR were significantly higher than the FP case over a smaller area. Figure 18b shows that the difference in downstream surface pressure distribution between the FP and BOR is small. Both follow the same trend with nearly the same magnitudes up to ambient pressure where the BOR distribution overshoots slightly more than the FP distribution. In both cases, the overshoot is generated by the reflected shock from the Mach disk coalesced with the compression waves generated by the growth of the far field wake vortices intersecting the downstream surface. Nonetheless, these distributions and wave formations indicate that the region downstream of the jet was the same despite the differences in geometry.

Although the geometries were different, the λ shock creating the attachment node upstream of the jet and the jet overexpansion downstream were similar and had the most significant impact on the surface pressures and JI force and moment. Integration of the surface pressures showed that the jet force and moment coefficients, C_{Nji} and C_{mji}, were significantly different as shown in Table 2 which compares the force, moment and thrust coefficients as well as the amplification coefficients for the BOR and FP calculations.

Table 2 Coefficients for FP and BOR, *PR*=2000

Body	C_{Nji}	C_{mji}	C_T	ε_N	ε_m	$L_{ref}(ft)$	$S_{ref}(ft^2)$
FP	-3.95e-3	+3.87e-3	-1.83e-2	+1.22	+0.46	1.5	2.25
BOR	+0.38	+2.37	-2.75	+0.86	+0.76	0.139	0.015

The jet interaction force and moment coefficients and thrust coefficients for the BOR were significantly different because of the referenced areas, S_{ref}, for the FP and BOR. However, the amplification coefficients between the two bodies were comparable and Table 2 shows the jet force was attenuated in the BOR case while it was amplified in the FP case which can be attributed to the surface pressure perturbations wrapping around the side of the body. The jet moment however was attenuated in both cases with FP attenuated more than twice as much as the BOR.

IV. Conclusions

The features of the Champigny-Lacau model for supersonic freestreams were verified, namely the bow shock, barrel shock, λ-shock, Mach disk, and horseshoe vortices. However, this study uncovered new flow structures downstream of the jet for both geometries, namely near-field and far-field wake vortices, a series of compression

waves and a downstream shock reflection which caused the overshoot in the downstream pressure distribution. These flow structures manifest themselves in surface pressure perturbations as well as significant modifications to the performance coefficients. For the FP geometry, JI amplified the jet thrust by more than 20% while it was attenuated the BOR jet thrust by less than 20%. The jet moment was attenuated for both geometries. The jet moment was attenuated more than 50% for the FP geometry, but less than 25% for the BOR geometry. The manifestation of the flow structures in surface pressure perturbations resulted in significant modification of the performance coefficients. The dramatic impact on JI performance characteristic illustrates the importance of understanding the extent of near field mean flow structure of transverse jets on the body under considered.

V. References

1. Margason, R.J., "Fifty Years of Jet in Cross Flow Research," AGARD 72nd FDP Meeting, Paper No. 1, 1993.
2. Ferrari, C., "Interference Between a Jet Issuing Laterally from a Body and the Enveloping Supersonic Stream," JPL Bumblebee Series, Report No. 286, April 1959.
3. Spaid, F.W., "A Study of Secondary Injection of Gases into a Supersonic Flow," Ph.D. Dissertation, California Institute of Technology, 1964.
4. Spaid, F.W. and Cassel, L.A.,"Aerodynamics Interference Induced by Reaction Controls," AGARDograph No. 173, Dec 1973.
5. Morkovin, M.V., Pierce, C.A., Jr, Cravens, C.E., "Interaction of a Side Jet With a Main Stream," *University of Michigan Press, Engineering Research Institute Bulletin No. 35*, 1952.
6. Cubbison, R.W., Anderson, B.H. and Ward, J.J., "Surface Pressure Distributions with a Sonic Jet Normal to Adjacent Flat Surfaces at Mach 2.92 to 6.4," NASA-TN-D-580, February 1961.
7. Fric, T.F. and Roshko, A., "Vortical Structure in the Wake of a Jet," *Journal of Fluid Mechanics, Vol. 279, pp. 1-47*, 1994.
8. Roger, R.P. and Chan, S.C., "CFD Study of the Flowfield Due to a Supersonic Jet Exiting into a Hypersonic Stream From a Conical Surface," AIAA Paper 93-2926, 1993.
9. Champigny, P. and Lacau, R.G., "Lateral Jet Control for Tactical Missiles," Special Course On Missile Aerodynamics, AGARD-R-804, Paper No. 3, 1994.
10. Gruber, M.R., Nejad, A.S., Chen, T.H. and Dutton, J.C., "Mixing and Penetration Studies of Sonic Jets in a Mach 2 Freeestream," *Journal of Propulsion and Power*, Vol. 11, No. 2, pp 315-323, 1995.
11. Dickmann, D.A. and Lu, F.K., "Jet in Supersonic Crossflow on a Flat Plate," AIAA-2006-3451, 2006.
12. Smith, B.R., "The *k-kl* Turbulence Model and Wall Layer Model for Compressible Flows," AIAA Paper 90-1483, June 1990.
13. Wilcox, D.C., *Turbulence Modeling for CFD*, DCW Industries, La Cañada, California, 2nd ed., 1998.
14. Shutts, W.H., Hartwig, W.H. and Weiler, J.E., "Final Report On Turbulent Boundary Layer And Skin Friction Measurements on a Smooth, Thermally Insulated Flat Plate at Supersonic Speeds," University of Texas, Defense Research Laboratory Report 364, 1955.
15. Mabey, D.G., Meier, H.U. and Sawyer, W.G., "Experimental and Theoretical Studies of the Boundary Layer on a Flat Plate at Mach Numbers from 2.5 to 4.5," RAE TR 74127, 1974.
16. Fernholtz, H.H. and Finley, P.J., "A Critical Compilation of Compressible Turbulent Boundary Layer Data," AGARDograph No. 223, June 1977.
17. Lu, F.K., "Fin Generated Shock-Wave Boundary-Layer Interactions," *Ph.D. Dissertation*, Pennsylvania State University, May 1988.
18. White, F.W., *Fluid Mechanics*, McGraw-Hill, New York, 1979.
19. Hopkins, E.J. and Inouye, M., "An Evaluation of Theories for Predicting Turbulent Skin Friction and Heat Transfer on Flat Plates at Supersonic and Hypersonic Mach Number," *AIAA Journal*, Vol. 9, No. 6, pp. 993-1003, 1971.
20. Dowdy, M.W. and Newton, J.F., "Investigation of Liquid and Gaseous Secondary Injection Phenomena on a Flat Plate with M = 2.01 and M = 4.54," JPL-TR-32-542, Dec. 1963.
21. Shapiro, A.H., *The Dynamics and Thermodynamics of Compressible Fluid Flow*, Vol II, Wiley, Inc., 1954.
22. Tobak, M. and Peake, D.J., "Topology of Three-Dimensional Separated Flow," *Annual Review of Fluid Mechanics*, Vol. 14, pp. 61-85, 1982.